Real-gas effects on aerodynamic bearings

Eliott Guenat[1], Jürg Schiffmann

Ecole Polytechnique Fédérale de Lausanne, EPFL STI IGM LAMD, Maladière 71b, CP 526, CH-2002 Neuchâtel 2

Abstract

Motivated by the use of aerodynamic bearings lubricated with high-pressure gases in energy conversion cycles, the Reynolds equation is adapted in order to include effects of real-gas and turbulence. Three geometries (Rayleigh-step slider, plain and herringbone-grooved journal bearing) serve to investigate real-gas effects on the static and dynamic properties with a wide variety of lubricants and nondimensional operating conditions. Computational results show a depreciation of the load capacity of journal bearings, with cases reaching a reduction of 50% with unequally affected force components. Stability can be affected both positively and negatively. Some stability losses reach nearly 100%, while improvements of several orders of magnitude with the grooved bearing are reported. Results are fluid-independent for similar reduced pressure and temperature.

Keywords: Aerodynamic Lubrication, Gas Bearings, Real Gas, Simulation

[1]Corresponding author. Email adress: eliott.guenat@epfl.ch

Roman symbols

A	Matrix containing density-independent terms of the discretized Reynolds equation
a	Groove length
b	Ridge length
C	Damping coefficient
c_s	NGT coefficient
D	Bearing diameter
e	Eccentricity
f	NGT coefficient
$G_\perp$	Turbulence correction factor perpendicular to the direction of motion
$G_\parallel$	Turbulence correction factor parallel to the direction of motion
g	NGT coefficient
H	Groove depth ratio
h	Clearance
h_0	Nominal clearance
h_g	Groove clearance
L	Bearing length
M	Matrix containing density-associated terms of the discretized Reynolds equation
M_c	Critical mass
M_r	Critical mass ratio
P	Pressure
P_c	Critical pressure
P_r	Reduced pressure
R	Radius
r	Specific gas constant
Re	Reynolds number
T	Temperature
T_C	Critical temperature
T_r	Reduced temperature
t	Time
U	Bearing tangential velocity
W	Load capacity
W_r	Load capacity ratio
X	Coordinate in the direction of the displacement
x	Coordinate in the inertial frame
y	Coordinate in the inertial frame

z	Axial coordinate
Z	Impedance, compressibility factor
	Greek symbols
α	Groove aspect ratio
β	Bulk modulus
$\hat{\beta}$	Groove angle
ϵ	Eccentricity ratio
θ	Circumferential coordinate
κ	Numerical relaxation coefficient
Λ	Compressibility number
μ	Dynamic viscosity
ρ	Density
σ	Squeeze number
Ω	Bearing angular velocity
ω	Excitation velocity
	Superscripts
$-$	Normalized
$*$	Modified
(10%)	10%-deviation
	Subscripts
a	Ambient condition
c	Critical
g	Groove
ig	Ideal-gas
l	Local
r	Ridge, ratio, reduced
rg	Real-gas
T	Constant temperature
x	x-axis
y	y-axis
z	z-axis
0	Static, unperturbed
1	Perturbed
	Acronyms
HC	Hydrocarbon
$HCFC$	Hydrochlorofluorocarbons
HFC	Hydrofluorocarbon

$HGJB$	Herringbone grooved journal bearing
PJB	Plain journal bearing
NGT	Narrow groove theory

1. Introduction

High-speed small-scale turbomachinery is likely to play an increasingly important role in the efficiency improvement of distributed energy conversion systems [1]. This technology is called to play a significant role as heat pump compressors [2], Organic Rankine Cycles expanders [3] and fuel cell gas recirculator [4]. Some of these applications typically involve high pressure and high temperature working fluids, possibly close to the critical point. Among the different bearing technologies, aerodynamic bearings are well suited to these application since they allow an oil-free high-lifetime operation, limiting the use of seals and keeping the system simple.

1.1. Nature of the issue

Historically, aerodynamic bearings were designed by solving the Reynolds equation under the assumption of an ideal gas lubricant [5]. Recent works have implemented the real-gas effects in the Reynolds equation in order to complete their bearing models, however, with a limited investigation of the qualitative or quantitative differences between the ideal- and real-gas lubrication. Schiffmann and Favrat[6] investigated the real-gas effects on the properties of herringbone-grooved journal bearings (HGJB) using the Narrow Groove Theory (NGT) and addressed the consequences on the optimal design of such bearings. They observed that the real-gas effects can have a negative influence on the stability and change the optimal geometry. Conboy [7] simulated a foil thrust gas bearing lubricated with CO_2 with the Reynolds equation including real-gas effects, however without investigating the effects of this consideration on the performance of the final design. Xu and Kim [8] developed a thermoelastic model applied on a foil thrust bearing lubricated with CO_2 and R245fa, including real-gas effects. They showed that the real-gas consideration reduces the peak-pressure in the fluid film, however in moderated proportions due to the high temperature of the fluid film in the investigated cases. Fairuz and Jahn [9] investigated the real-gas effects on dry seals using a bulk-flow model and found that the real-gas effects were beneficial for the sealing properties thank to the increased density. In general, prior work lacks of generalization regarding the role of both the lubricant and the operating conditions. In addition, an in-depth description of the effects of real gas on the bearing performance, and their consequences on bearing design are missing.

1.2. Goals and objectives

This present work aims to (1) address the real-gas effects on different aerodynamic bearing geometries both for static and dynamic performance on a wide range of operating conditions, (2) investigate these effects with multiple working fluids in a large domain of reduced temperature and pressure and (3) express the results in terms of nondimensional numbers in order to ensure a high level of generality.

1.3. Scope of the Paper

The Reynolds equation is adapted to express the density field in aerodynamic bearings, with the bulk modulus as a parameter accounting for the real-gas effect. The perturbation method is applied to obtain the dynamic properties of the fluid film. The ratios of actual critical mass and load capacity with regards to the ideal-gas lubrication serves as metrics for the characterization of the real-gas effects on a Rayleigh step slider bearing, a plain journal bearing (PJB) and a HGJB. 10 fluids of different chemical nature (HCFC, HFC, HC and natural working fluids) are investigated on a wide range of operating conditions with the use of reduced temperature and pressure, compressibility number and ambient Reynolds number as nondimensional parameters.

2. Theory

The pressure distribution in an aerodynamic bearing is modeled by using the Reynolds equation under the assumption of a thin fluid film (properties are lumped across the film thickness), isoviscosity, negligible inertia effects and Newtonian fluids. Since real-gas effects are associated with high-density fluids, the Reynolds number in the bearing can reach a level where turbulence has to be included in the constitutive lubrication equation. In order to account for the laminar-turbulent transition, correction terms are added to the Reynolds equation according to prior work suggesting expressions for these terms [10] [11] [12]. The Reynolds equation with the turbulence correction terms is given as follows:

$$\partial_X \left(\frac{\rho G_\perp h^3}{12\mu} \partial_X P \right) + \partial_z \left(\frac{\rho G_\parallel h^3}{12\mu} \partial_z P \right) = \frac{U}{2} \partial_X (\rho h) + \partial_t (\rho h) \qquad (1)$$

The first two terms correspond to the Poiseuille flow contribution, whereas the third one includes the driving Couette flow. The last term describes

the squeeze film effect. $G_\perp$ and $G_\parallel$ are the turbulence correction terms. Correlations suggested by Constantinescu [10] are used in this work since they are valid for both smooth and discontinuous surfaces:

$$G_\parallel = (1 + 0.001133 Re^{0.9})^{-1} \tag{2}$$

$$G_\perp = (1 + 0.000358 Re^{0.96})^{-1} \tag{3}$$

where $Re = U\rho h/\mu$. This correlation is valid for $1000 < Re < 30000$. For laminar flows, $G_\parallel = G_\perp = 1$. The ambient Reynolds number is introduced in order to compare different bearings operating in similar conditions:

$$Re_a = \frac{U\rho_a h_0}{\mu} \tag{4}$$

where ρ_a corresponds to the density at ambient conditions, U the surface velocity and h_0 the nominal clearance.

In the historical approach of solving this non-linear differential equation, the ideal gas law $P = \rho r T$ is usually applied under the assumption of isothermal compression [5], thus simplifying the approximation of a solution. In order to account for real gas effects, ρ can be computed from the value of P and T using a fluid database, which will indeed integrate the desired effects, however, without highlighting the dominating parameters involved in the real-gas behavior. Hence, the following substitution is proposed for the pressure derivative terms in the Poiseuille flow terms of Reynolds equation:

$$\frac{\partial P}{\partial X} = \left(\frac{\partial P}{\partial \rho}\right)_T \cdot \frac{\partial \rho}{\partial X} \tag{5}$$

the parameter $(\partial_\rho P)_T$ is linked to the bulk modulus:

$$\rho \left(\frac{\partial P}{\partial \rho}\right)_T = \beta \tag{6}$$

The Reynolds equation is nondimensionalized using the following substitutions:

$$\begin{gathered} \bar{\rho} = \rho/\rho_a \quad \bar{P} = P/P_a \quad \bar{\beta} = \beta/P_a \quad \theta = X/R \\ \bar{z} = z/R \quad \bar{h} = h/h_0 \quad \bar{t} = t\omega \end{gathered} \tag{7}$$

leading to the nondimensionalized Reynolds equation that includes both turbulence and real-gas effects (Figure A.1):

$$\begin{aligned}\partial_\theta\left(\bar{\beta}G_{\parallel}\bar{h}^3\partial_\theta\bar{\rho}\right)+\partial_{\bar{z}}\left(\bar{\beta}G_{\perp 0}\bar{h}^3\partial_{\bar{z}}\bar{\rho}\right)\\ =\Lambda\partial_\theta\left(\bar{\rho}\bar{h}_0\right)+\sigma\partial_{\bar{t}}\left(\bar{\rho}\bar{h}_0\right)\end{aligned} \tag{8}$$

Λ and σ are the compressibility and squeeze numbers respectively, defined as follows for journal bearings:

$$\Lambda=\frac{6\mu UR}{P_a h_0^2}=\frac{6\mu\Omega R^2}{P_a h_0^2} \tag{9}$$

$$\sigma=2\Lambda\frac{\omega}{\Omega} \tag{10}$$

Note that equation 8 is free from pressure terms and contains only the density and the derivative term $(\partial_{\bar{\rho}}\bar{P})_T$ incorporated in the bulk modulus $\bar{\beta}$. This last term accounts for the real gas effects and equals 1 for an ideal gas:

$$(\partial_{\bar{\rho}}\bar{P})_T=\frac{\rho_a}{P_a}(\partial_\rho P)_T=\frac{\rho_a rT}{P_a}=1 \tag{11}$$

Furthermore, this parameter equals 0 for a real gas at its critical point. Under the assumptions of isothermal compression and isoviscosity, the knowledge of this parameter is sufficient to characterize the real-gas effect of any gas lubricant on the density field. The steady-state form of Equation 8 can be solved numerically using a central finite difference scheme and boundary conditions set depending on the bearing geometry. The discretization leads to a system of equations written as follows:

$$M(\vec{\rho})\cdot\vec{\rho}=\vec{A}(\vec{\rho}) \tag{12}$$

where $\vec{\rho}$ is the nondimensional density distribution within the fluid film, $M(\vec{\rho})$ is the matrix containing the Poiseuille and Couette flows terms together with the density-related boundary conditions terms and $\vec{A}(\vec{\rho})$ is the vector containing the boundary conditions terms free from the density. The equation is solved iteratively starting from a guessed nondimensional density field, usually assumed to be 1 for each node. At each iteration, the system of equation is solved to find the density as follows:

$$\vec{\rho}^{(n+1)}=\vec{\rho}^{(n)}+\kappa\cdot\left(M^{-1}(\vec{\rho}^{(n)})\cdot\vec{A}(\vec{\rho}^{(n)})-\vec{\rho}^{(n)}\right) \tag{13}$$

where $0<\kappa\leq 1$ is a numerical relaxation coefficient easing convergence. The terms in matrix $M(\vec{\rho})$ are updated based on the last density

field. The terms $(\partial_{\bar{\rho}}\bar{P})_T$ are computed for each node of the domain using a fluid database [13]. The iterative process is stopped when a convergence threshold is reached:

$$\left| \frac{\bar{\rho}_k^{(n)} - \bar{\rho}_k^{(n-1)}}{\bar{\rho}_k^{(n-1)}} \right| < 10^{-4} \quad \forall k \in \{1..N\} \tag{14}$$

where N is the number of nodes in the domain. In order to compute the bearing reaction forces, the resulting density field is converted to pressure as follows:

$$P_k = Z_k \rho_k r T \tag{15}$$

where the compressibility factor Z evaluated at each node by using the fluid database.

In the case of journal bearings, stability is a major design objective that has to be satisfied, which often dominates load capacity as design constraint. A metric to characterize the bearing stability is the critical mass. Its computation requires the knowledge of the linearized dynamic parameters of the bearing (stiffness and damping) resulting from a harmonic perturbation around its static equilibrium position. The Reynolds equation in cylindrical coordinates is recalled:

$$\partial_\theta \left(\bar{\beta} G_\parallel \bar{h}^3 \cdot \partial_\theta \bar{\rho} \right) + \partial_{\bar{z}} \left(\bar{\beta} G_\perp \bar{h}^3 \cdot \partial_{\bar{y}} \bar{\rho} \right) = \Lambda \partial_\theta (\bar{\rho}\bar{h}) + \sigma \partial_{\bar{t}} (\bar{\rho}\bar{h}) \tag{16}$$

The clearance is perturbed by an infinitesimal harmonic motion ϵ_{1x} and ϵ_{1y} in the x and y directions respectively [14]:

$$\bar{h} = \bar{h}_0 + \epsilon_{0x} \cos\theta + \epsilon_{0y} \sin\theta + \epsilon_{1x} \cos\theta e^{i\bar{t}} + \epsilon_{1y} \sin\theta e^{i\bar{t}} \tag{17}$$

where ϵ_{0x} and ϵ_{0y} are the static equilibrium eccentricity ratio. The harmonic clearance perturbation results in a perturbation of the density $\bar{\rho}$, the bulk modulus $\bar{\beta}$ and the turbulence correction terms:

$$\bar{\rho} = \bar{\rho}_0 + \epsilon_{1x} \bar{\rho}_{1x} e^{i\bar{t}} + \epsilon_{1y} \bar{\rho}_{1y} e^{i\bar{t}} \tag{18}$$

$$\bar{\beta} = \bar{\beta}_0 + \epsilon_{1x} \left(\frac{\partial \bar{\beta}}{\partial \bar{\rho}} \right)_0 \bar{\rho}_{1x} e^{i\bar{t}} + \epsilon_{1y} \left(\frac{\partial \bar{\beta}}{\partial \bar{\rho}} \right)_0 \bar{\rho}_{1y} e^{i\bar{t}} \tag{19}$$

$$G = G_0 + \epsilon_{1x} \left(\left(\frac{\partial G}{\partial \bar{\rho}} \right)_0 \bar{\rho}_{1x} e^{i\bar{t}} + \left(\frac{\partial G}{\partial \bar{h}} \right)_0 \cos\theta e^{i\bar{t}} \right) \tag{20}$$

$$+ \epsilon_{1y} \left(\left(\frac{\partial G}{\partial \bar{\rho}} \right)_0 \bar{\rho}_{1y} e^{i\bar{t}} + \left(\frac{\partial G}{\partial \bar{h}} \right)_0 \sin\theta e^{i\bar{t}} \right) \tag{21}$$

All terms of order higher than 1 are discarded and only terms of order 0 and 1 are retained. Equations 22 and 23 group zeroth-order terms and first-order terms with respect to ϵ_{1x}. The first-order perturbed equation in the y direction is obtained following the same method.

$$\begin{aligned} \partial_\theta \left[\bar{\beta}_0 G_{\parallel 0} \bar{h}_0^3 \partial_\theta \bar{\rho}_0\right] + \partial_{\bar{z}} \left[\bar{\beta}_0 G_{\perp 0} \bar{h}_0^3 \partial_{\bar{z}} \bar{\rho}_0\right] \\ -\Lambda \partial_\theta \left(\bar{\rho}_0 \bar{h}_0\right) = 0 \end{aligned} \tag{22}$$

$$\begin{aligned} \partial_\theta \Bigg[\left(\frac{\partial \bar{\beta}}{\partial \bar{\rho}}\right)_0 \bar{\rho}_1 G_{\parallel 0} \bar{h}_0^3 \partial_\theta \bar{\rho}_0 + \\ \bar{\beta}_0 \left(\left(\frac{\partial G_\parallel}{\partial \bar{\rho}}\right)_0 \bar{\rho}_{1x} + \left(\frac{\partial G_\parallel}{\partial \bar{h}}\right)_0 \cos\theta \right) \bar{h}_0^3 \partial_\theta \bar{\rho}_0 + \\ \bar{\beta} G_{\parallel 0} 3 \bar{h}_0^2 \cos\theta \partial_\theta \bar{\rho}_0 + \bar{\beta}_0 G_{\parallel 0} \bar{h}_0^3 \partial_\theta \bar{\rho}_{1x} \Bigg] \\ + \partial_{\bar{z}} \Bigg[\left(\frac{\partial \bar{\beta}}{\partial \bar{\rho}}\right)_0 \bar{\rho}_1 G_{\perp 0} \bar{h}_0^3 \partial_{\bar{z}} \bar{\rho}_0 + \\ \bar{\beta}_0 \left(\left(\frac{\partial G_\perp}{\partial \bar{\rho}}\right)_0 \bar{\rho}_{1x} + \left(\frac{\partial G_\perp}{\partial \bar{h}}\right)_0 \cos\theta \right) \bar{h}_0^3 \partial_{\bar{z}} \bar{\rho}_0 + \\ \bar{\beta} G_{\perp 0} 3 \bar{h}_0^2 \cos\theta \partial_\theta \bar{\rho}_0 + \bar{\beta}_0 G_{\perp 0} \bar{h}_0^3 \partial_\theta \bar{\rho}_{1x} \Bigg] \\ -\Lambda \partial_\theta \left(\bar{\rho}_0 \cos\theta + \bar{\rho}_{1x} \bar{h}_0\right) - i\sigma \left(\bar{\rho}_0 \cos\theta + \bar{\rho}_{1x} \bar{h}_0)\right) = 0 \end{aligned} \tag{23}$$

The zeroth-order equation is solved using the numerical procedure described in Equations 12 to 14. The boundary conditions are:

- Ambient conditions at the lateral sides: $\bar{\rho}_0 = 1$ at $\bar{z} = \pm L_z/D$
- Periodicity of the density field: $\bar{\rho}_0(\theta, \bar{z}) = \bar{\rho}_0(\theta + 2\pi, \bar{z})$

The boundary conditions for the perturbed equation are :

- Ambient conditions at the lateral sides: $\bar{\rho}_{1x} = 0$ at $\bar{z} = \pm L_z/D$
- Periodicity of the density field: $\bar{\rho}_{1x}(0, \bar{z}) = \bar{\rho}_{1x}(2\pi, \bar{z})$

The load capacity W is computed from the static pressure field from the reaction force acting on the bearing in both directions:

$$W_x = -R^2 P_a \int_{-L_z/D}^{L_z/D} \int_0^{2\pi} \bar{P}_0 \cos\theta \mathrm{d}\theta \mathrm{d}\bar{z} \tag{24}$$

$$W_y = -R^2 P_a \int_{-L_z/D}^{L_z/D} \int_0^{2\pi} \bar{P}_0 \sin\theta \mathrm{d}\theta \mathrm{d}\bar{z} \tag{25}$$

$$W = \sqrt{W_x^2 + W_y^2} \tag{26}$$

The equations regrouping terms of first order are linear with respect to the perturbed density. After discretization following a central finite difference scheme, the systems of linear equations in the x and y directions can be written as follows and solved straightforwardly:

$$M_x \vec{\rho}_{1x} = \vec{A}_x \tag{27}$$

$$M_y \vec{\rho}_{1y} = \vec{A}_y \tag{28}$$

The perturbed pressure field is obtained from the density following as follows:

$$\bar{P}_{1x/y} = \left(\partial_{\bar{\rho}} \bar{P}\right)_{T,0} \bar{\rho}_{1x/y} \tag{29}$$

The bearing impedances $Z_{a,b} = K_{a,b} + i\omega C_{a,b}$ are obtained as follows:

$$Z_{xx} = -R^2 P_a \int_{-L_z/D}^{L_z/D} \int_0^{2\pi} \bar{P}_{1x} \cos\theta \mathrm{d}\theta \mathrm{d}\bar{z} \tag{30}$$

$$Z_{yx} = -R^2 P_a \int_{-L_z/D}^{L_z/D} \int_0^{2\pi} \bar{P}_{1x} \sin\theta \mathrm{d}\theta \mathrm{d}\bar{z} \tag{31}$$

$$Z_{yy} = -R^2 P_a \int_{-L_z/D}^{L_z/D} \int_0^{2\pi} \bar{P}_{1y} \sin\theta \mathrm{d}\theta \mathrm{d}\bar{z} \tag{32}$$

$$Z_{xy} = -R^2 P_a \int_{-L_z/D}^{L_z/D} \int_0^{2\pi} \bar{P}_{1y} \cos\theta \mathrm{d}\theta \mathrm{d}\bar{z} \tag{33}$$

The critical mass is computed by searching for the excitation frequency ω canceling the imaginary part of the equivalent impedance Z of the system:

$$Im(Z(\omega)) = 0 \tag{34}$$

where Z is given as follows:

$$Z = \frac{1}{2}(Z_{xx} + Z_{yy}) \pm \sqrt{\frac{1}{4}(Z_{xx} - Z_{yy})^2 + Z_{xy}Z_{yx}} \tag{35}$$

At the particular excitation frequency ω_c, the following is obtained:

$$Z = M_c\omega_c^2 \tag{36}$$

where M_c is the critical mass of the system.

The same method for obtaining the static and dynamic properties can be applied for HGJB using the NGT. Hsing [15] derived the NGT applied to HGJB including correction terms in order to account for the turbulence in the lubrication film. The equations are equivalent to the laminar form of the theory when G terms accounting for turbulence are set to 1 [16]. This procedure models the overall "smooth pressure" generated by an infinite number of groove-ridge pairs over the bearing domain. The resulting differential equation is recalled here:

$$\begin{aligned} \partial_\theta\left[\bar{\rho}\left(f_1\partial_\theta\bar{P} + f_2\partial_{\bar{z}}\bar{P}\right)\right] + \partial_{\bar{z}}\left[\bar{\rho}\left(f_2\partial_\theta\bar{P} + f_3\partial_{\bar{z}}\bar{P}\right)\right] \\ +c_s\left(\sin\hat{\beta}\partial_\theta(f_4\bar{\rho}) - \cos\hat{\beta}\partial_{\bar{z}}(f_5\bar{\rho})\right) \\ -\Lambda\partial_\theta(f_6\bar{\rho}) - \sigma\partial_{\bar{t}}(f_6\bar{\rho}) = 0 \end{aligned} \tag{37}$$

where the geometry is presented in Figure A.2 and the functions f are summarized in the Appendix. A first-order perturbation is applied to this equation following Equations 17 to 21 and zeroth- and first-order equations are segregated to be solved successively with the same numerical scheme indicated above.

3. Results and discussion

The model developed above is applied for different geometries of aerodynamic bearings in order highlight the real-gas effects on the lubrication performance in terms of load capacity and stability.

3.1. Infinitely wide step slider bearing

The steady-state form of Equation 8 is solved for an infinitely wide step slider bearing operating at $\Lambda = 3$ and 10 , assuming a laminar regime in the thin film. In the case of slider bearings (Figure A.3), Λ is defined as follows:

$$\Lambda = \frac{6\mu U L_x}{P_a h_0^2} \tag{38}$$

The boundary conditions are $\bar{\rho} = 1$ at $\bar{x} = 0$ and $\bar{x} = 1$, where $\bar{x} = X/L_x$. The lubricant is R134a (a typical heat pump working fluid) at reduced ambient conditions corresponding to $T_r = T_a/T_c = 1$ and $P_r = P_a/P_c = 0.5$. The pressure distributions for ideal gas and real gas are compared in Figure A.4. The real gas consideration leads to a redistribution of the pressure, with a lowered peak pressure compared to the pressure when the ideal-gas law is assumed. For $\Lambda = 3$, the pressure of the real gas reaches a slightly higher value than the ideal one for $\bar{x} \in [0.5, 1]$, leading to an overall load capacity increased by 1%. The load capacity in its nondimensional form is defined by Equation 39.

$$\bar{W} = \int_0^1 (\bar{P} - 1) \mathrm{d}\bar{x} \tag{39}$$

At $\Lambda = 10$, this increased pressure zone (as a result of real-gas effects) is confined to $\bar{x} \in [0.8, 1]$ and is negatively compensated by a lowered pressure in the remaining domain, resulting in a load capacity 8.5% lower than the ideal gas case.

Figure A.5 shows the evolution of the nondimensional load capacity with the compressibility number for the considered slider bearing lubricated with R134a and highlights the compressibility effects associated with real gas consideration. The temperature is fixed to the critical value while the relative pressure is varied. The ideal-gas case shows that the load capacity evolves linearly for small compressibility numbers before deviating to reach a limit value corresponding to the solution for $\Lambda \to \infty$. The linear domain is due to the quasi-incompressiblity of the lubricant at low speed. This linear range is affected by the real gas effects. The points A, B and C in Figure A.5 indicate the location where a 10%-difference between the actual load capacity and the one predicted by the incompressible solution occurs. As the pressure is increased toward the critical value, the real-gas effects get amplified and the 10%-difference location is shifted toward smaller compressibility numbers. The real-gas effects in the sub-critical domain increase the compressibility of the fluid, since the parameter $(\partial_\rho P)_T$ decreases as the critical point is approached. This has the effect to shift the appearance of compressibility effects to lower compressibility numbers compared to the ideal-gas behavior, thus narrowing the validity of the quasi-incompressible behavior. The value of $\Lambda^{(10\%)}$ corresponding to the 10%-deviation point can be estimated within a 2%-error interval using Equation 40.

$$\Lambda_{rg}^{(10\%)} = \Lambda_{ig}^{(10\%)} \cdot (\partial_{\bar{\rho}} \bar{P})_{T,a} \tag{40}$$

Thus, this equation can help to estimate the validity domain of the incompressible-solution in real-gas lubrication based on the ideal-gas case.

This bearing configuration is simulated for a wide range of ambient conditions with the following parameter serving as a metric to compare the real- and ideal-gas load capacity:

$$W_r = \frac{W_{rg}}{W_{ig}} \tag{41}$$

Figures A.6 and A.7 represent the iso-W_r lines for R134a at $\Lambda = 1$ and $\Lambda = 10$ respectively. The cases close to the saturation line achieving saturation conditions inside the gas film are discarded, thus leaving an empty space between the saturation line and the isolines. At constant pressure, a reduction of the temperature increases the influence of the real gas consideration, so does an increase in pressure at constant temperature. The deviation from the ideal-gas lubrication increases with the compressibility number, which has the effect of shifting the isolines to lower pressure levels. Note that at $\Lambda = 1$ real-gas effects tend to increase the load capacity, whereas at $\Lambda = 10$ it is decreases significantly.

Figure A.8 shows the difference between the maximum and the minimum value of W_r for a given ambient condition among 10 working fluids of different chemical nature, including both synthetic and natural fluids (R123, R134a, R170, R22, R245fa, R290, R600a, R717, R718, R744) at $\Lambda = 10$. The term *composite saturation curve* indicates the saturation curve bounding the phase change of the 10 considered refrigerants. The maximum deviation in load capacity within the considered domain is below 4% in this case and below 1% for $\Lambda = 1$, which allows to conclude that the load capacity of a step slider bearing is nearly independent of the nature of the fluid if the reduced ambient conditions are known. Further, a representation in the reduced pressure and reduced temperature domain is suggested to be sufficient to adequately map the real-gas effects in a gas-lubricated slider bearings.

3.2. Plain Journal Bearing

The same approach in the $P_r - T_r$ domain is applied to a PJB operating at an eccentric position with a length over diameter ratio L_z/D of 1. Simulations considering real- and ideal-gas lubrication in laminar regime are compared using the ratio of load capacity W_r (Equation 39) and the ratio of critical mass M_r as performance metrics, where M_r is defined such as:

$$M_r = \frac{M_{c,rg}}{M_{c,ig}} \tag{42}$$

Results for the load capacity ratio are presented in Figures A.9 and A.10 for compressibility number 1 and 10 respectively, simulating a bearing at an eccentricity ratio $\epsilon = e/h_0$ of 20% and lubricated with R134a. As observed with the slider bearing at high compressibility number, real-gas effects negatively affect the load capacity and become more significant as the compressibility number Λ increases. The evolution of W_r with the compressibility number for three different ambient conditions is shown in Figure A.11, which emphasizes this observation. The load capacity ratio diverges quickly from unity before reaching a limit value for high Λ, corresponding to the limit solution for $\Lambda \to \infty$. The limit value depends on the distance of the ambient conditions from the critical point, the point of highest P_r being the most affected by the real-gas effects. Figure A.12 presents the pressure profile at the mid-span of the PJB at an eccentricity ratio of 0.6 along the x-axis, lubricated with R134a at $P_r = 0.75$, $T_r = 1$ and $\Lambda = 1$. The pressure is affected both in amplitude and distribution, leading to load components unequally affected by the real-gas consideration: the radial component drops by 8.5% and the tangential one by 45 %, resulting in a reduction of total load capacity of 28 % compared to the ideal-gas case. As a consequence of this unequal change in load distribution, the attitude angle is affected and brought to lower absolute values, as shown in Figure A.13. The reduction of the attitude angle is an indication of an increased stability as a result of the real-gas effects.

Figures A.14 and A.15 depict the evolution of the critical mass ratio M_r for $\Lambda = 1$ and 10 respectively. Interestingly, real-gas effects appear to have a positive influence at low compressibility numbers that vanishes, however, at high compressibility numbers. The evolution of the critical mass ratio for three ambient conditions against the compressibility number Λ is presented in Figure A.16 and shows a monotonically decreasing trend starting from values well above unity. At $\Lambda \approx 2$ the critical mass ratio reaches approximately 1 for the three operating conditions, the unity threshold being postponed to slightly higher compressibility numbers as the distance from critical point increases.

The similarity between refrigerants in the $P_r - T_r$ domain remains verified with PJBs, for both considerations of stability and load capacity, as presented in Figures A.17 and A.18, where the maximum deviation between fluids is reported for each ambient condition at $\Lambda = 10$ and $\epsilon_x = 0.2$. The maximum deviation observed between the same 10 fluids as previously cited remains below 4% for both metrics. Increasing the eccentricity ratio to 0.5 does not change the value of the maximum observed deviation.

3.3. Herringbone-Grooved Journal Bearings

A full HGJB with the grooved member rotating is analyzed following the same strategy as for the PJB. The geometry is inspired from the optimal design computed by Flemming and Hamrock [17] for $\Lambda = 1$. The groove depth over clearance ratio h_g/h_r at a concentric position is 2, the groove angle $\hat{\beta}$ is 150°, the groove aspect ratio α is 0.5 and the length over diameter ratio L_z/D is 1. The flow regime is laminar. Figure A.19 shows the ratio of critical mass for the considered bearing at concentric position and $\Lambda = 1$, using R134a. Qualitatively, the trend is comparable to the PJB. Interestingly, a line of very high stability is suggested to appear above a certain value of compressibility number, where the critical mass computed under the real-gas consideration tends to infinity. In such cases, the condition of Equation 34 is satisfied for a whirl frequency ω of very small values, while the amplitude of the equivalent impedance is not significantly affected. As a result, a very high critical mass is obtained (Equation 36). The position of these lines is presented in Figure A.20. The lines are shifted toward higher T_r and lower P_r as the compressibility number increases. For low values of Λ, the line interferes with the saturation line and is no longer observable. At constant pressure and increasing temperature, M_r is first below unity, then reaches the point of maximum stability and finally decays asymptotically to unity at very high temperatures. This behavior is presented in Figure A.22 for $P_r = 0.5$ and R134a for different values of Λ and in Figure A.21 for different ambient conditions at fixed Λ. Note the relatively large range of ambient conditions where real-gas effects yield to an increased stability compared to the ideal-gas lubrication case.

The same behavior is observed for the 10 working fluids mentioned previously. Figure A.23 represents the positions of the maximum stability for each fluid at $\Lambda = 10$, with R170 and R245fa which bound the other fluids. All the lines are confined in a domain whose width grows with reduced pressure, which suggests that the similarity between fluids loses its validity when the HGJB operating conditions approach the critical pressure. In this zone, the quantitatively small deviation between fluids observed previously is not verified for HGJB because of the strong slopes observed in Figure A.22, where a small deviation in the position along T_r results in a very significant deviation in M_r.

Regarding the real-gas effects on the load capacity of HGJB, the trend is linear against Λ beyond a certain value, as shown in Figure A.24. The

convergence toward a limiting solution as seen with the PJB in Figure A.11 is not present here, because of the hypothesis behind the NGT. The quasi-incompressible NGT relies on the assumption of a constant pressure gradient between each groove-ridge pair, strictly valid for an incompressible lubricant only. Constantinescu showed that this assumption is valid even at relatively large values of Λ in the case of HGJB. However, due to the enhanced compressibility induced by the real-gas effects, the validity domain of the NGT is narrowed, which is supported by Figure A.5 for a step bearing. Therefore, results from the NGT around the critical point should be treated with caution, even at moderated values of Λ. Constantinescu introduced the local compressibility number Λ_l, defined as follows:

$$\Lambda_l = \bar{h}_g^2 \alpha \frac{a+b}{L} \Lambda \sin^2 \hat{\beta} \tag{43}$$

He suggested $\Lambda_l = 0.1 - 0.15$ as threshold values of compressibility effects. Employing the observation made for the slider bearing in Equation 40, the threshold can be adapted for real-gas lubrication with the use of Equation 40:

$$\Lambda_{l,rg} = \bar{h}_g^2 \alpha \frac{a+b}{L} \frac{\Lambda}{(\partial_{\bar{\rho}} \bar{P})_{T,a}} \sin^2 \hat{\beta} \tag{44}$$

The threshold of $\Lambda_{l,rg} = 0.1 - 0.15$ can be assumed to estimate the limit of validity of quasi-incompressible NGT in real-gas lubrication.

3.4. Real-gas effects with turbulence

Effects of turbulence are implemented by using Constantinescu's correction terms. Figure A.25 presents the evolution of W_r for an eccentric PJB as a function of Λ for three different values of ambient Reynolds numbers Re_a. The drop in load capacity ratio due to the real-gas effects observed in laminar regime occurs more sharply and at lower compressibility numbers with increasing ambient Reynolds numbers. Qualitatively, the real-gas effects are not significantly affected compared to the laminar lubrication. In substance, turbulence tends to enhance the real-gas effects. A similar observation is valid for the critical mass ratio shown in Figure A.26, although the trend in turbulent regime differs after the initial drop since M_r recovers linearly after the extremum, thus achieving improved values of M_r past a particular value of Λ. It has to be noted that the critical mass and load capacity ratios are defined for equal ambient Reynolds numbers.

The region of very high critical mass ratio observed for HGJB still exists in the turbulent regime. The behavior of M_r on both sides of this region is not qualitatively affected, however the position of the line in the $P_r - T_r$ domain depends on the ambient Reynolds number. Figure A.27 shows the evolution of M_r with the reduced temperature at constant reduced pressure and compressibility number. For the particular operating condition (Λ, P_r), the point of local peak stability is not visible in the laminar regime but appears as the ambient Reynolds numbers increases, thus shifting the position of the extremum toward higher reduced temperature, such as symbolically illustrated in Figure A.28. Thus, compared to the laminar flow regime, the domain where $M_r < 1$ is expanded. As a result of turbulence, a safe bearing design is more difficult to achieve.

The use of another correlation for the turbulence correction terms is not expected to influence the results significantly, since they systematically lead to a reduced Poiseuille flow and, as a results, an increased overall density in the fluid film domain which amplifies the real-gas effects.

4. Conclusions

The Reynolds equation was expressed in terms of density instead of pressure, with the appearance a thermodynamic parameter addressing real-gas effects. Static and dynamic resolutions of this equation were performed on different bearing geometries and led to the following observations:

1. Real-gas effects strongly depend on the value of the reduced pressure P_r and temperature T_r. Proximity of the critical point amplifies real-gas effects in bearings
2. In general, real-gas effects negatively affect the load capacity of journal bearings (PJB and HGJB), although a 6%-increase was computed for a step slider bearing at a low value of Λ
3. Depending on the operating and ambient conditions, the critical bearing mass is either positively or negatively affected by the real-gas effects. At moderated values of Λ, the effect is positive on PJB, but becomes negative beyond a threshold value of $\Lambda \approx 2$. For HGJB, the critical mass ratio can reach very high values along a line in the $P_r - T_r$ domain. Its position depends on the value of Λ.
4. Deviation from the ideal-gas behavior evaluated for a particular fluid is valid for other fluids of diverse chemical nature with a moderated

error for PJB and step slider bearing. This is observed as long as the similitude of geometry, compressibility number and reduced temperature and pressure is verified. This agreement between different fluids is also observed for HGJB, where lines of high stability appear in the same region of the $P_r - T_r$ domain, although the absolute value of the deviation is large near these high-stability regions.

5. The validity of the incompressible solution to the Reynolds equation is limited to lower values of Λ due to the rising effect of real gas. The threshold of validity can be estimated from the ambient value of the parameter accounting for real-gas effects and the ideal-gas threshold. By extension, a modified threshold of validity for the quasi-incompressible NGT based on [18] is suggested for real-gas lubrication of HGJB.
6. The presence of turbulence enhances the real-gas effects on both the load capacity and the stability. The drop in load capacity ratio is more pronounced at low compressibility numbers and the regions of high stability observed for HGJB are shifted to higher reduced temperature and lower reduced pressure.

Considering these observations, the position of the operation point in the $P_r - T_r$ domain is suggested to be the most relevant design variable when designing a gas bearing-rotor system. Because of the high pressure build-up in HGJB, particular care should be taken in the design of such bearings in order to take advantage of the real-gas effects and avoid their possible negative influence. The real-gas effects tend to phase out at high reduced temperature and low reduced pressure.

Acknowledgment

The authors would like to thank Mr. Shalash for countless fruitful discussions. The authors aknowledge the funding through the EPFL.

Reference

[1] J. Schiffmann, D. Favrat, Design, experimental investigation and multi-objective optimization of a small-scale radial compressor for heat pump applications, Energy 35 (2010) 436–450.

[2] A. Javed, C. Arpagaus, S. Bertsch, J. Schiffmann, Small-scale turbocompressors for wide-range operation with large tip-clearances for a

two-stage heat pump concept, International Journal of Refrigeration 69 (2016) 285–302.

[3] J. Demierre, A. Rubino, J. A. Schiffmann, Modeling and Experimental Investigation of an Oil-Free Microcompressor-Turbine Unit for an Organic Rankine Cycle Driven Heat Pump, Transactions- ASME Journal of Engineering for Gas Turbines and Power 137 (2015) 032602.

[4] P. H. Wagner, Z. Wuillemin, S. Diethelm, J. Van Herle, J. Schiffmann, Modeling and Designing of a Radial Anode Off-Gas Recirculation Fan for Solid Oxide Fuel Cell Systems, Journal of Electrochemical Energy Conversion and Storage 14 (2017) 011005.

[5] D. D. Fuller, A Review of the State-of-the-Art for the Design of Self-Acting Gas-Lubricated Bearings, Journal of Lubrication Technology 91 (1969) 1–16.

[6] J. Schiffmann, D. Favrat, The effect of real gas on the properties of Herringbone Grooved Journal Bearings, Tribology International 43 (2010) 1602–1614.

[7] T. M. Conboy, Real-Gas Effects in Foil Thrust Bearings Operating in the Turbulent Regime, Journal of Tribology 135 (2013) 031703–031703–12.

[8] F. Xu, D. Kim, Three-Dimensional Turbulent Thermo-Elastohydrodynamic Analyses of Hybrid Thrust Foil Bearings Using Real Gas Model (2016) V07BT31A030.

[9] Z. Fairuz, I. Jahn, The influence of real gas effects on the performance of supercritical CO 2 dry gas seals, Tribology International 102 (2016) 333–347.

[10] V. N. Constantinescu, Basic Relationships in Turbulent Lubrication and Their Extension to Include Thermal Effects, Journal of Lubrication Technology 95 (1973) 147–154.

[11] G. G. Hirs, A Bulk-Flow Theory for Turbulence in Lubricant Films, Journal of Lubrication Technology 95 (1973) 137–145.

[12] C.-W. Ng, C. H. T. Pan, A Linearized Turbulent Lubrication Theory, Journal of Basic Engineering 87 (1965) 675–682.

[13] I. H. Bell, J. Wronski, S. Quoilin, V. Lemort, Pure and Pseudo-pure Fluid Thermophysical Property Evaluation and the Open-Source Thermophysical Property Library CoolProp, Industrial & Engineering Chemistry Research 53 (2014) 2498–2508.

[14] J. W. Lund, Calculation of Stiffness and Damping Properties of Gas Bearings, Journal of Lubrication Technology 90 (1968) 793–803.

[15] F. C. Hsing, Formulation of a Generalized Narrow Groove Theory for Spiral Grooved Viscous Pumps, Journal of Lubrication Technology 94 (1972) 81–85.

[16] J. H. Vohr, C. Y. Chow, Characteristics of Herringbone-Grooved, Gas-Lubricated Journal Bearings, Journal of Basic Engineering 87 (1965) 568–576.

[17] D. P. Fleming, B. J. Hamrock, Optimization of self-acting herringbone-grooved journal bearings for maximum stability, 1974.

[18] V. N. Constantinescu, V. Castelli, On the Local Compressibility Effect in Spiral-Groove Bearings, Journal of Lubrication Technology 91 (1969) 79–86.

Appendix A. Turbulent NGT

The terms composing equation 37 are developed here.

$$\bar{h}_r = \frac{h_r}{h_0} = \frac{h_r}{h_r(\epsilon = 0)} \tag{A.1}$$

$$\bar{h}_g = \frac{h_g}{h_0} \tag{A.2}$$

$$H = \frac{h_g(\epsilon = 0)}{h_0} \tag{A.3}$$

$$\begin{aligned} g_{1z} =& \bar{h}_g^3 \bar{h}_r^3 [(1-\alpha)(\cos^2\hat{\beta} G_{zg} + \sin^2\hat{\beta} G_{\theta g}) G_{zr} + \\ & \alpha(\cos^2\hat{\beta} G_{zr} + \sin^2\hat{\beta} G_{\theta r}) G_{zg}] \end{aligned} \tag{A.4}$$

$$\begin{aligned} g_{1\theta} =& \bar{h}_g^3 \bar{h}_r^3 [(1-\alpha)(\cos^2\hat{\beta} G_{zg} + \sin^2\hat{\beta} G_{\theta g}) G_{\theta r} + \\ & \alpha(\cos^2\hat{\beta} G_{zr} + \sin^2\hat{\beta} G_{\theta r}) G_{\theta g}] \end{aligned} \tag{A.5}$$

$$g_2 = (\bar{h}_g^3 G_{zg} - \bar{h}_r^3 G_{zr})(\bar{h}_g^3 G_{\theta g} - \bar{h}_r^3 G_{\theta r}) \alpha(1-\alpha) \tag{A.6}$$

$$\begin{aligned} g_3 =& (1-\alpha)\bar{h}_g^3(\cos^2\hat{\beta} G_{zg} + \sin^2\hat{\beta} G_{\theta g}) + \\ & \alpha \bar{h}_r^3(\cos^2\hat{\beta} G_{zr} + \sin^2\hat{\beta} G_{\theta r}) \end{aligned} \tag{A.7}$$

$$c_s = -\frac{6\mu\Omega R^2}{p_a h_0^2} \alpha(1-\alpha)(H-1) \tag{A.8}$$

$$f_1 = \frac{g_{1\theta} + g_2 \sin^2\hat{\beta}}{g_3} \tag{A.9}$$

$$f_2 = \frac{g_2 \sin\hat{\beta}\cos\hat{\beta}}{g_3} \tag{A.10}$$

$$f_3 = \frac{g_{1z} + g_2 \cos^2\hat{\beta}}{g_3} \tag{A.11}$$

$$f_4 = \frac{\bar{h}_g^3 G_{\theta g} - \bar{h}_r^3 G_{\theta r}}{g_3} \tag{A.12}$$

$$f_5 = \frac{\bar{h}_g^3 G_{zg} - \bar{h}_r^3 G_{zr}}{g_3} \tag{A.13}$$

$$f_6 = \alpha \bar{h}_g + (1-\alpha)\bar{h}_r \tag{A.14}$$

List of Figures

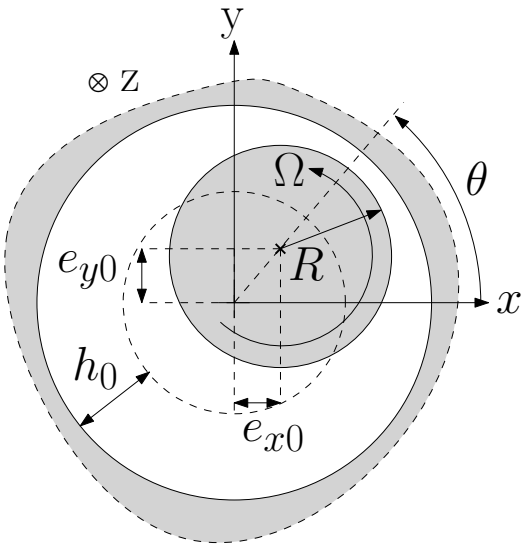

Figure A.1: Geometry and nomenclature of a journal bearing

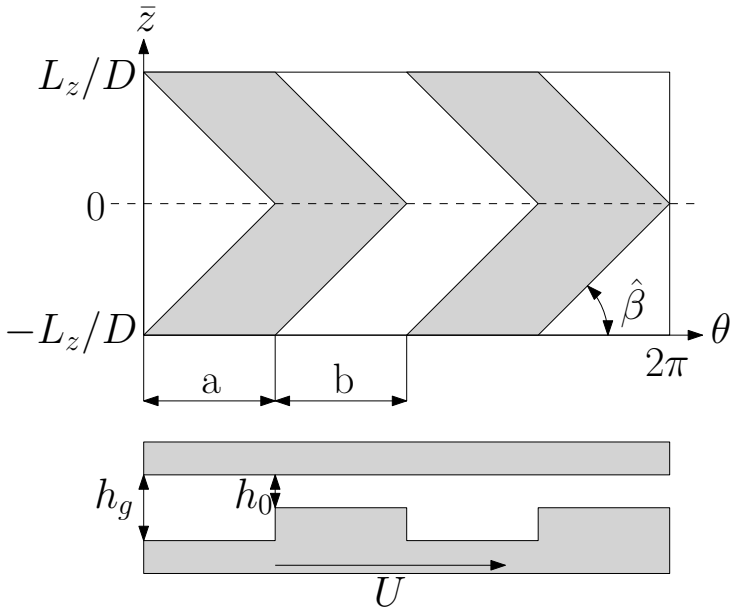

Figure A.2: Geometry and nomenclature of a HGJB

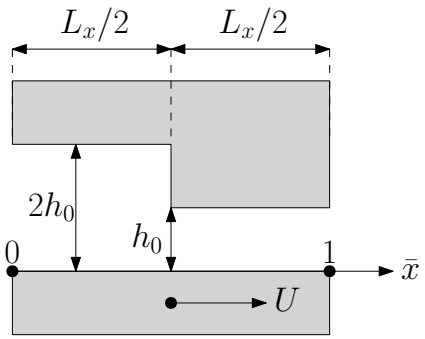

Figure A.3: Geometry of the studied step bearing

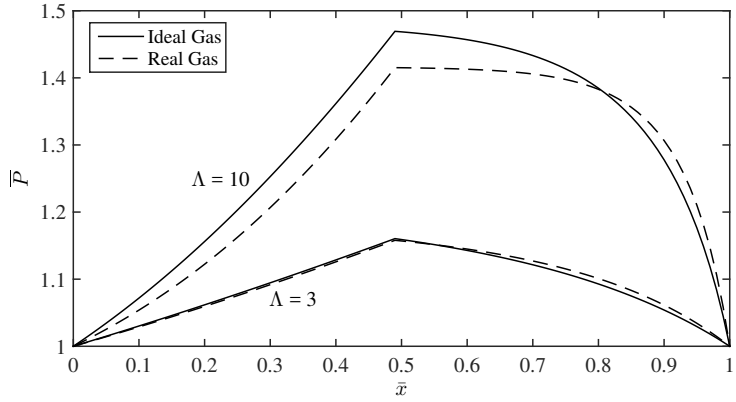

Figure A.4: Comparison of pressure distribution in a step slider bearing for two compressibility numbers, with R134a at $T_r = 1$, $P_r = 0.5$

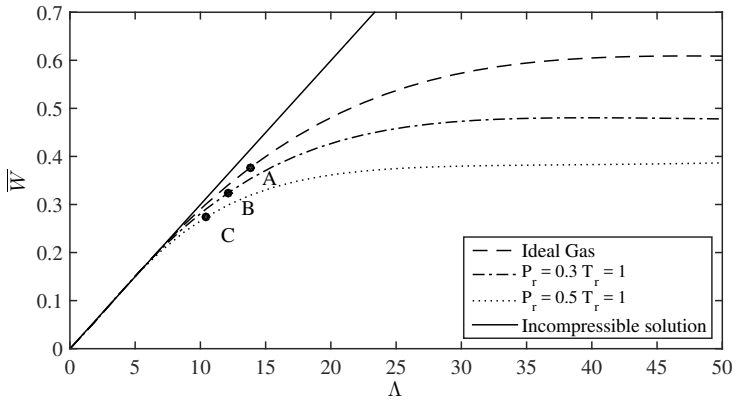

Figure A.5: Evolution of the nondimensional load capacity of an infinitely wide Rayleigh step bearing as a function of Λ for R134a. The dots indicate the points of a 10%-deviation from the incompressible solution

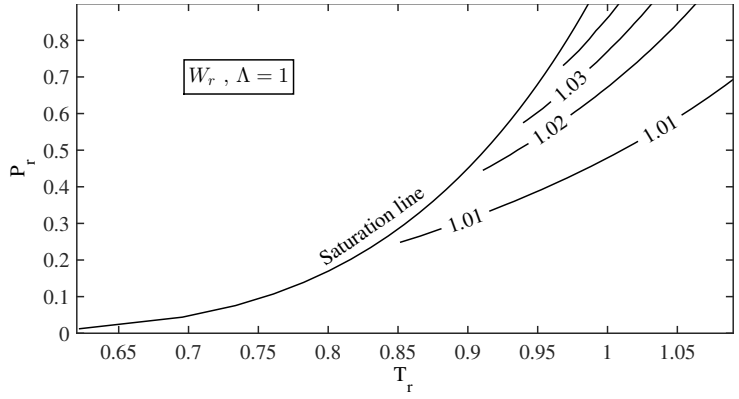

Figure A.6: Isolines of W_r for a step slider bearing at $\Lambda = 1$ with R134a

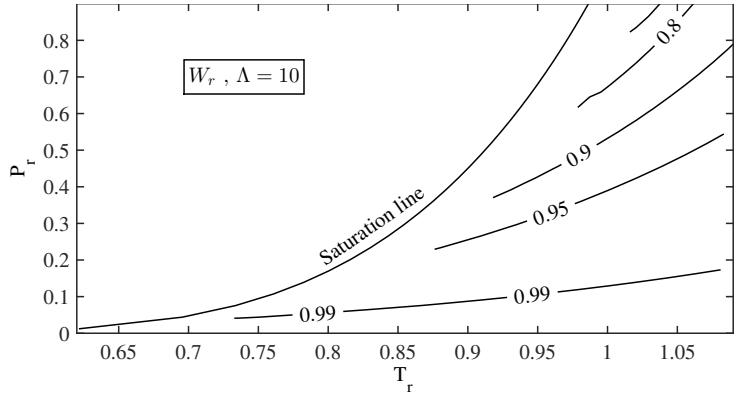

Figure A.7: Isolines of W_r for a step slider bearing at $\Lambda = 10$ with R134a

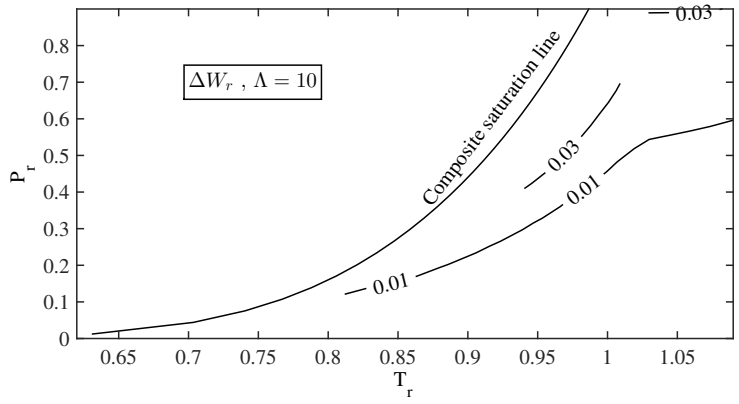

Figure A.8: Isolines of maximum deviation of W_r between 10 different fluids for a step slider bearing at $\Lambda = 10$

as a function of reduced pressure and temperature

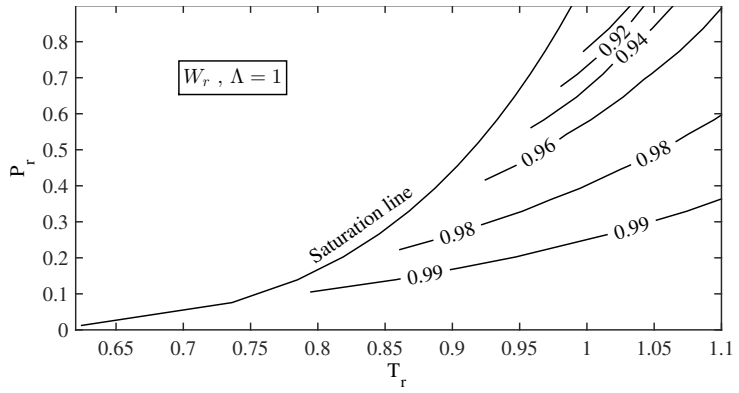

Figure A.9: Isolines of W_r for a PJB (ϵ_x=0.2, $\epsilon_y = 0$, R134a) at $\Lambda = 1$

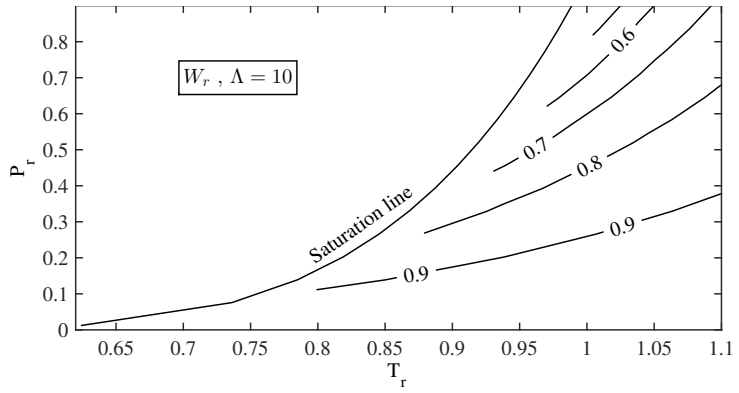

Figure A.10: Isolines of W_r for a PJB (ϵ_x=0.2, ϵ_y=0, R134a) at $\Lambda = 10$

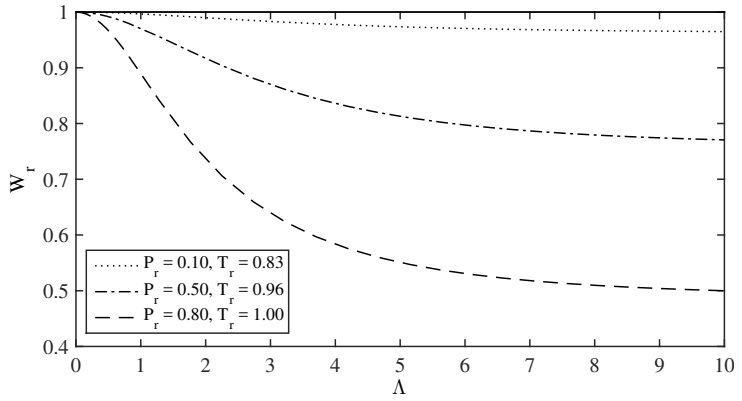

Figure A.11: Evolution of W_r with Λ for a PJB (ϵ_x=0.2, ϵ_y=0, R134a)

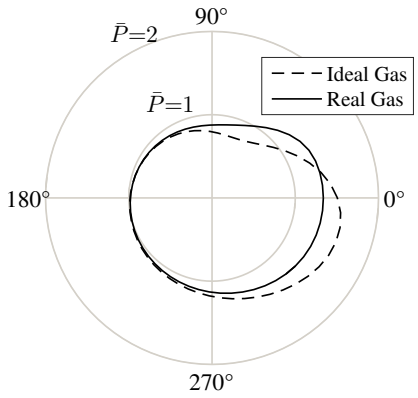

Figure A.12: Mid-span pressure profiles of a PJB (ϵ_x=0.6, ϵ_y=0) at $\Lambda = 1$ with R134a at $P_r = 0.75$ and $T_r = 1$

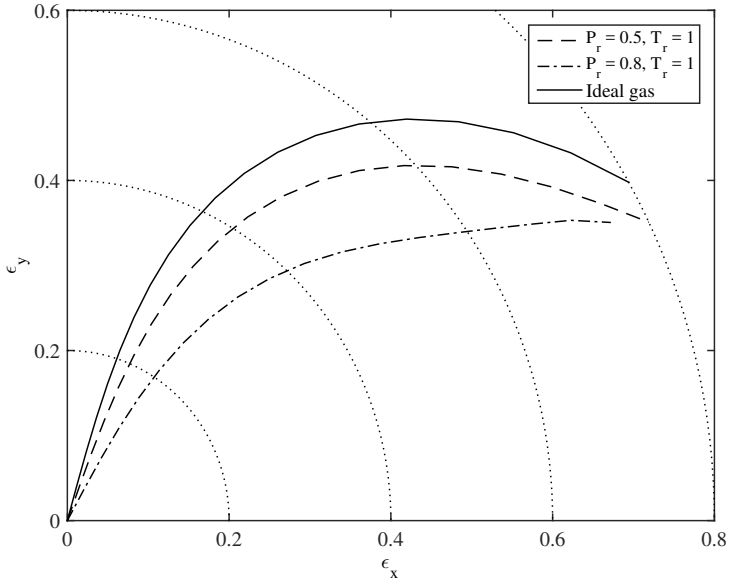

Figure A.13: Static locus of a PJB lubricated with R134a at $\Lambda = 1$ with a force along the x-axis

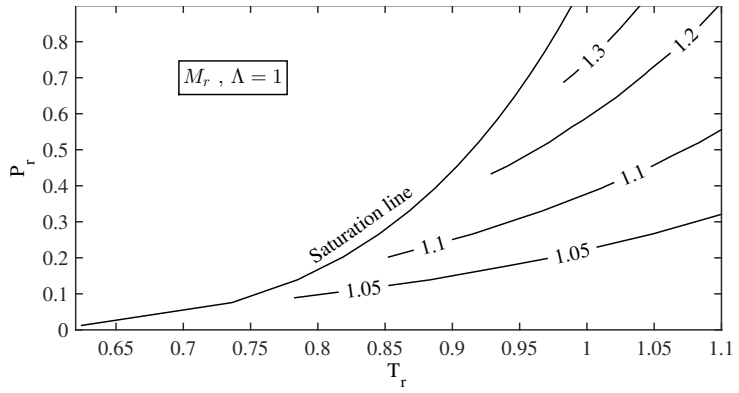

Figure A.14: Isolines of M_r for a PJB (ϵ_x=0.2, $\epsilon_y = 0$, R134a) at $\Lambda = 1$

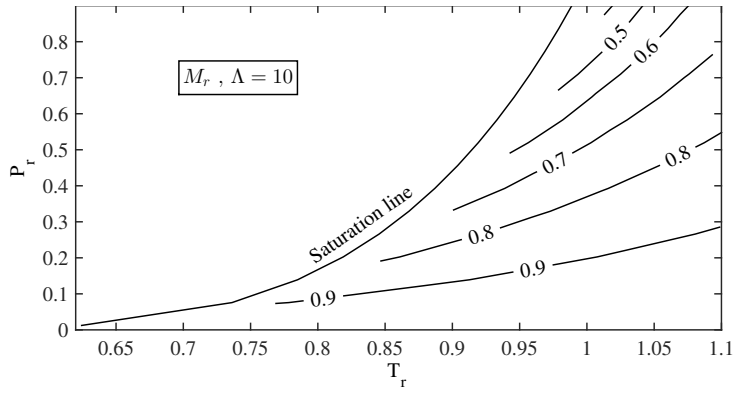

Figure A.15: Isolines of M_r for a PJB (ϵ_x=0.2, $\epsilon_y = 0$, R134a) at $\Lambda = 10$

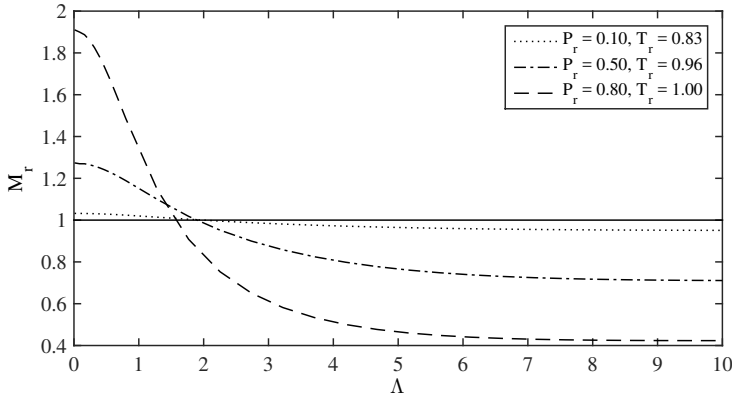

Figure A.16: Evolution of the critical mass ratio with the compressibility number for a PJB (R134a, ϵ_x=0.2, $\epsilon_y = 0$)

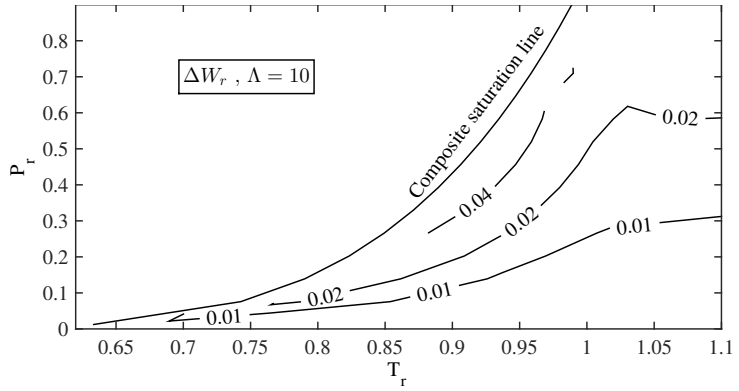

Figure A.17: Isolines of maximum deviation of W_r between 10 fluids for a PJB (ϵ_x=0.2, ϵ_y=0) at $\Lambda = 10$

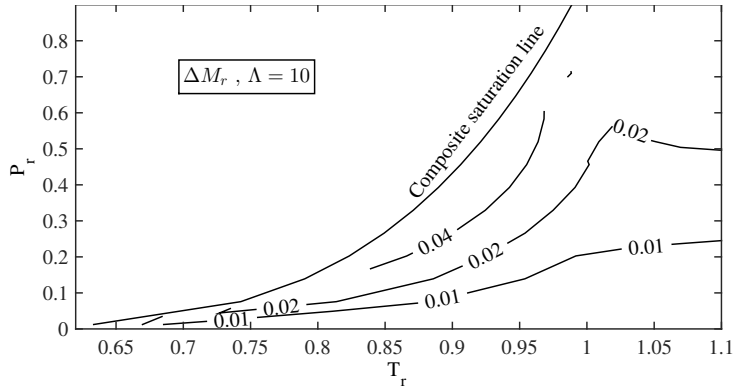

Figure A.18: Isolines of maximum deviation of M_r between 10 fluids for a PJB (ϵ_x=0.2, ϵ_y=0) at $\Lambda = 10$

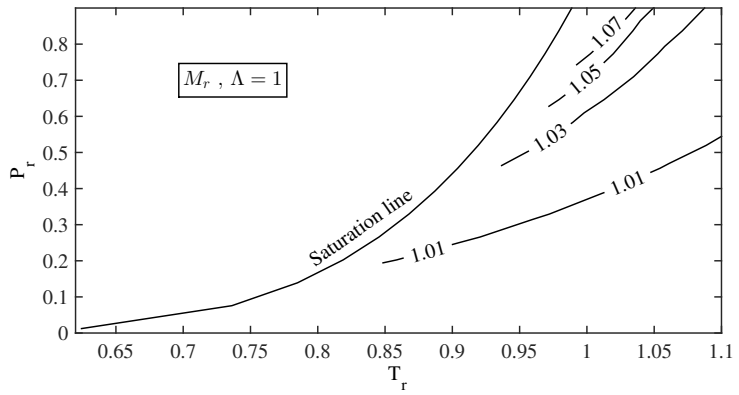

Figure A.19: Isolines of M_r for a HGJB (ϵ=0, R134a) at $\Lambda = 1$

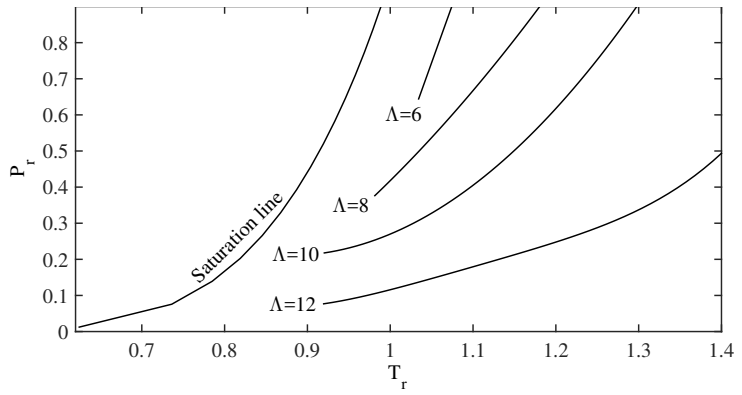

Figure A.20: Position of the lines of maximum stability for a HGJB (ϵ=0, R134a)

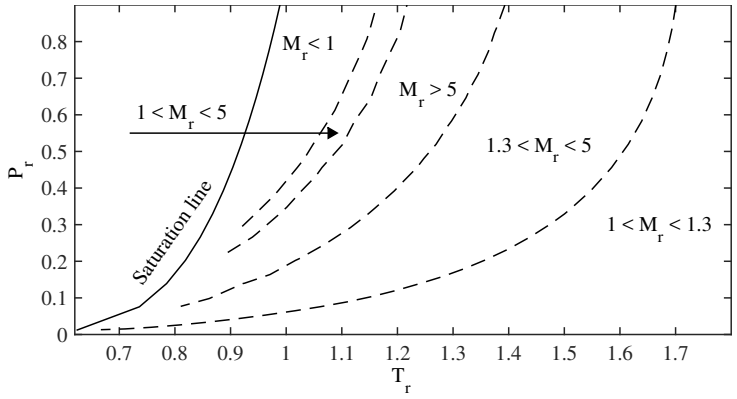

Figure A.21: Different domains of value of M_r for a HGJB (ϵ=0, R134a) at $\Lambda = 10$

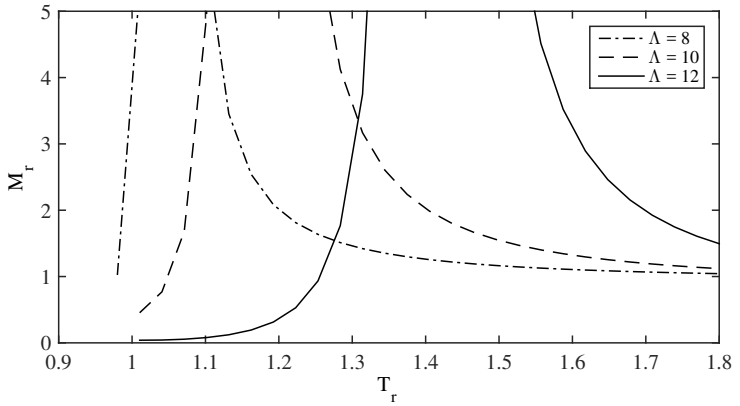

Figure A.22: Evolution of M_r with T_r at $P_r = 0.5$ (R134a, $\epsilon = 0$)

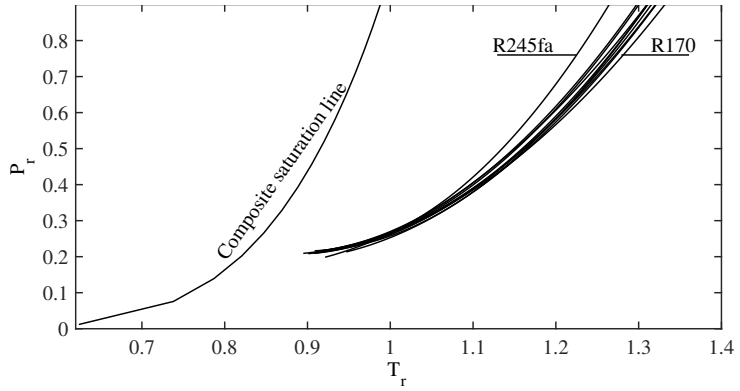

Figure A.23: Position of the lines of maximum M_r for HGJB lubricated with 10 different fluids at $\Lambda = 10$

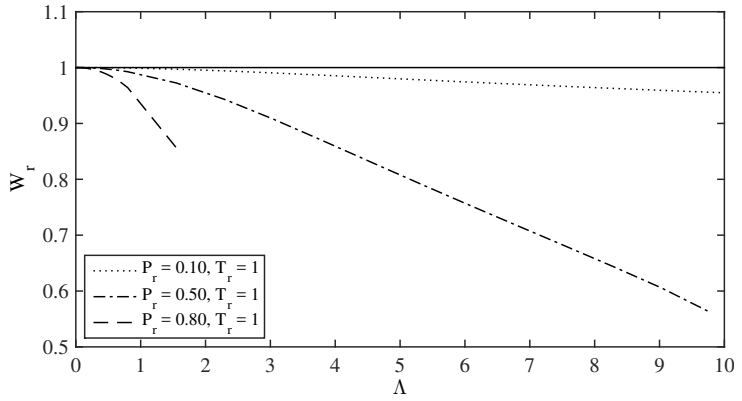

Figure A.24: Evolution of W_r with Λ for HGJB at $\epsilon_x = 0.2$, $\epsilon_y = 0$ (R134a)

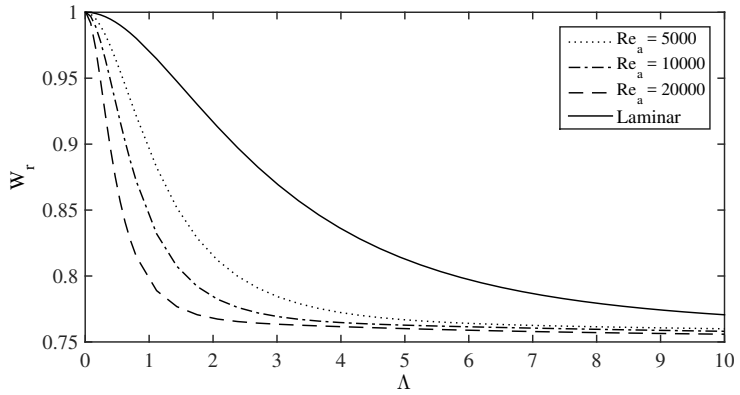

Figure A.25: Evolution of W_r for PJB at $\epsilon_x = 0.2$ with turbulent flow ($P_r = 0.5$, $T_r = 1$, R134a)

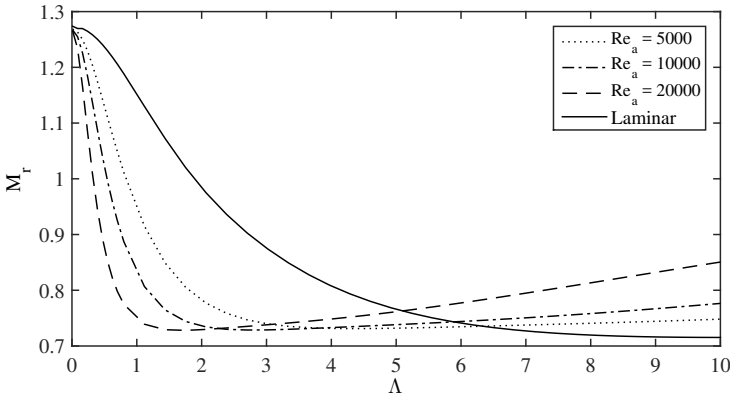

Figure A.26: Evolution of M_r for PJB at $\epsilon_x = 0.2$ with turbulent flow ($P_r = 0.5$, $T_r = 1$, R134a)

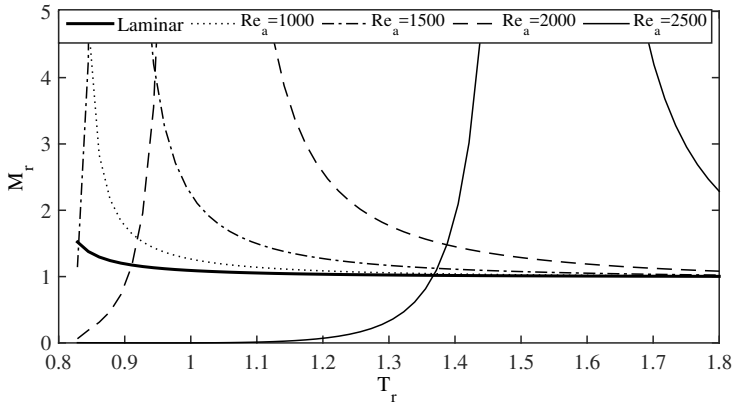

Figure A.27: Evolution of M_r for HGJB at $\epsilon = 0$ with different values of Re_a ($P_r = 0.2$, $\Lambda = 5$, R134a)

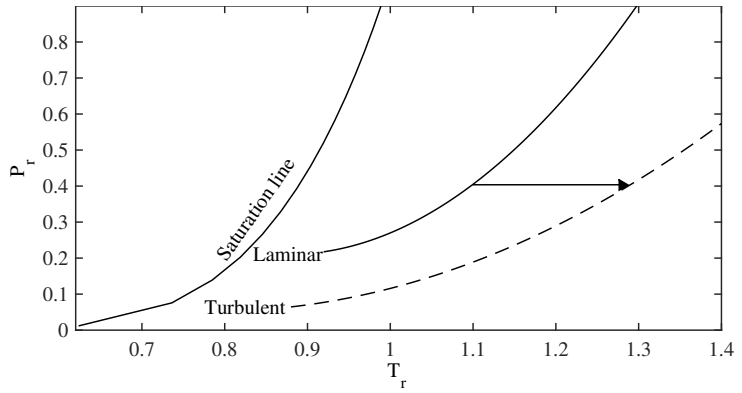

Figure A.28: Qualitative illustration of the evolution of the maximum stability line as the ambient Reynolds number increases for a given Λ